ChemComm

FEATURE ARTICLE

View Article Online
View Journal | View Issue

Cite this: *Chem. Commun.*, 2021, **57**, 2343

Recent advances in perovskite oxides as electrode materials for supercapacitors

Yang Cao,†[ab] Jie Liang,†[b] Xue Li,[a] Luchao Yue,[b] Qian Liu,[b] Siyu Lu,[c] Abdullah M. Asiri,[d] Jianming Hu,*[a] Yonglan Luo*[b] and Xuping Sun*[b]

Owing to the high power density and ultralong cycle life, supercapacitors represent an alternative to electrochemical batteries in energy storage applications. However, the relatively low energy density is the main challenge for supercapacitors in the current drive to push the entire technology forward to meet the benchmark requirements for commercialization. To effectively solve this issue, it is crucial to develop electrode materials with excellent electrochemical performance since the electrode used is closely related to the specific capacitance and energy density of supercapacitors. With the unique structure, compositional flexibility, and inherent oxygen vacancy, perovskite oxides have attracted wide attention as promising electrode materials for supercapacitors. In this review, we summarize the recent advances in perovskite oxides as electrode materials for supercapacitors. Firstly, the structures and compositions of perovskite oxides are critically reviewed. Following this, the progress in various perovskite oxides, including single perovskite and derivative perovskite oxides, is depicted, focusing on their electrochemical performance. Furthermore, several optimization strategies (*i.e.*, modulating the stoichiometry of the anion or cation, A-site doping, B-site doping, and constructing composites) to improve their electrochemical performance are also discussed. Finally, the significant challenges facing the advancement of perovskite oxide electrodes for supercapacitor applications and future outlook are proposed.

Received 8th December 2020,
Accepted 26th January 2021

DOI: 10.1039/d0cc07970g

rsc.li/chemcomm

1. Introduction

The energy paradigm has changed from an era of fossil fuel resources to sustainable energy sources and new technologies associated with energy conversion and storage to address the rapid depletion of fossil fuels. Currently, energy storage and conversion technologies mainly include batteries, fuel cells, and supercapacitors (SCs).[1–3] Among them, SCs have aroused considerable interest due to their high power density (>10 K W kg^{-1}), long cycle life ($>10^5$ cycles), and bridging function of the power/energy gap between traditional dielectric capacitors with high power output and batteries/fuel cells with high energy storage (Fig. 1).[4–7]

Based on the charge storage mechanism, SCs can be classified into two categories:[8] electrochemical double layer capacitors (EDLCs) and pseudocapacitors (PCs). EDLCs store charge through charge accumulation at the interface between the electrolyte and the electrode's surface. This process is a physical process without any electrochemical reaction (non-faradaic), guaranteeing fast energy uptake and delivery and avoiding the electrode materials' swelling. As such, EDLCs have high power density (>15 K W kg^{-1}) and long cycle life ($>10^5$ cycles).[9,10] Because of their high specific surface area (1000–3000 m^2 g^{-1}) and desirable conductivity, carbon-based materials (such as carbon nanotubes, activated carbon, and graphene) are the most attractive to date for EDLCs.[11] However, experimentally, owing to the finite conductivity and unavailability of all of the active sites, the practical specific capacitance of pure carbon-based EDLCs achieved has usually been limited to ~100–350 F g^{-1}.[12–14] In comparison to EDLCs, PCs store charge *via* reversible redox reaction (faradaic reaction) between the electrode materials and the electrolyte. Since the electrochemical reactions occur both on the surface and in the bulk near the solid electrode surface, PCs often show far higher capacitance values and energy density (by a factor of 10 or higher) than EDLCs.[15] Metal oxides

[a] *School of Physics and Electrical Engineering, Chongqing Normal University, Chongqing 401331, China. E-mail: hujianming@cqnu.edu.cn*
[b] *Institute of Fundamental and Frontier Sciences, University of Electronic Science and Technology of China, Chengdu 610054, Sichuan, China. E-mail: luoylcwnu@hotmail.com, xpsun@uestc.edu.cn*
[c] *Green Catalysis Center, and College of Chemistry, Zhengzhou University, Zhengzhou 450001, Henan, China*
[d] *Chemistry Department, Faculty of Science & Center of Excellence for Advanced Materials Research, King Abdulaziz University, P.O. Box 80203, Jeddah 21589, Saudi Arabia*
† Both authors contributed equally to this work.

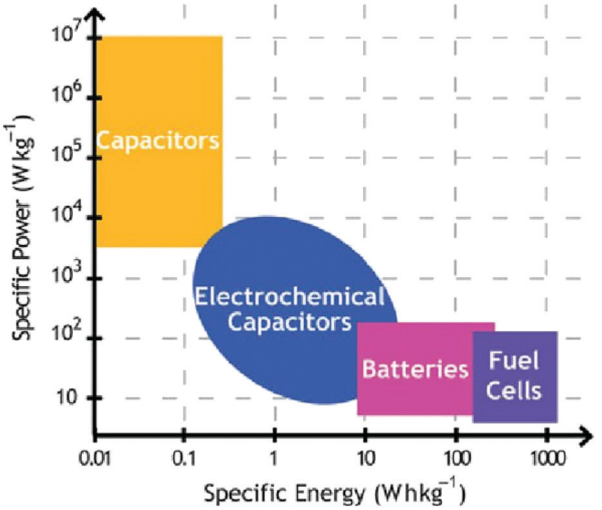

Fig. 1 Comparison of specific power *vs.* specific energy of capacitors and batteries. Reproduced from ref. 6 with permission from Materials Research Society, copyright 2011.

and conductive polymers typically work as electrode materials in PCs due to their fast reversible redox reactions, cost-effectiveness as well as easy processability.[16,17] Although PCs have a high energy density, they are not satisfactory in terms of power density and stability due to their poor electrical conductivity and framework swelling during cycling.[18] Therefore, achieving high energy density while maintaining the high power density of SCs has become a challenging task.

As per the calculation formula ($E = 1/2CV^2$), the energy capability of SCs is in proportion to the specific capacitance (C) and the square of voltage windows (V). Hence, the energy density can be improved by enhancing either the potential windows or the specific capacitance value. For the measurement of electrochemical response, electrochemical cells can be designed in either a half cell or a full cell configuration. The half cell is composed of three electrodes (working electrode, counter electrode, and reference electrode), while the full cell is composed of two electrodes (positive and negative electrodes).[19] Generally, the cell potential can be increased by assembling asymmetric electrodes (two different electrode materials for the anode and the cathode) or by using organic electrolytes.[19,20] Typically, in an aqueous-based symmetric system, the working voltage is limited to less than 1.2 V (due to the thermodynamic breakdown potential of water molecules).[21] Based on the same active material, when it is assembled into an asymmetric supercapacitor (ASC), the voltage window will be expanded to 2.5 V, while when using organic electrolytes, the potential window will be expanded to 3 V.[22,23] On the other hand, finding sustainable electrode materials is an effective strategy to improve the specific capacitance. Among the many candidate materials, metal oxides have attracted significant interest because they can provide higher energy density than conventional carbon materials and have better cycle lives than polymer materials.[24] With a wide potential window (about 1.2 V), excellent electronic conductivity (3×10^2 S cm^{-1}), and high theoretical specific capacitance (1358 F g^{-1}), RuO_2 is the most active electrode material.[25] Nonetheless, high cost and limited abundance restrict its widespread applications. In this context, non-noble metal oxides such as MnO_2, NiO, and Fe_3O_4 have been widely explored.[26–28] Nevertheless, some inherent shortcomings, such as low electrical conductivity and poor cycling stability, limit their practical applications.

As star materials, perovskite oxides have rapidly drawn intensive attention owing to their low cost, robust skeleton structure, high tap density, and inherent nature of containing oxygen vacancies and distinctive chemical tailoring.[29,30] Over the past few decades, perovskite oxides have traditionally been used as functional materials in energy-related fields. In 2014, a breakthrough work on the oxygen anion intercalation mechanism for nanostructured lanthanum-based perovskite oxides was reported by Meffold *et al.*[31] The mechanism is as follows: in the first step, the diffusion of oxygen is in the form of OH^- from the electrolyte. Subsequently, the oxygen vacancies are filled by OH^- groups and they diffuse along the octahedral edges through the crystal concomitant with the oxidation of two Mn^{2+} centers to two Mn^{3+} and yielding water as a product. In the next step of the reaction, excess oxygen is intercalated at the surface by diffusion of manganese to the surface and oxidation of two Mn^{3+} centers to two Mn^{4+} (Fig. 2).[31,32] As mentioned above, the bulk of perovskite oxide is involved in the storage of charge, which means that perovskite oxide does not require a high surface area to achieve high energy storage. There are metal oxides (such as TiO_2-B, T-Nb_2O_5, and α-MoO_3) with similar intercalation behavior to perovskite oxides but are based on positive ions (such as Li^+ or Na^+) as the charge carrier.[33–35] In principle, O^{2-} can carry two negative charges per unit, which means that the intercalation pseudocapacitance

Xuping Sun

Xuping Sun received his PhD degree from the Changchun Institute of Applied Chemistry (CIAC), Chinese Academy of Sciences, in 2006. During 2006–2009, he carried out postdoctoral research at Konstanz University, University of Toronto, and Purdue University. In 2010, he started his independent research career as a full Professor at CIAC and then moved to Sichuan University in 2015. In 2018, he joined the University of Electronic Science and Technology of China, where he found the Research Center of Nanocatalysis & Sensing. He was recognized as a highly cited researcher (2018–2020) in both areas of chemistry and materials science by Clarivate Analytics. He has published over 490 papers with total citations over 42 000 and an h-index of 108. His research mainly focuses on the rational design of functional nanostructures toward applications in electrochemistry for energy conversion and storage, sensing, and environment.

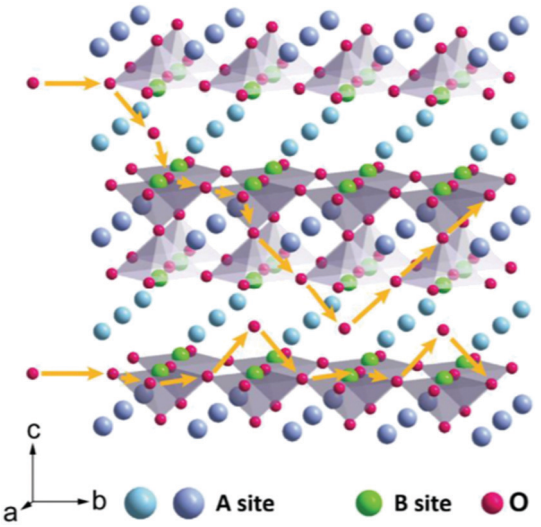

Fig. 2 Mechanism of oxygen intercalation into perovskite oxides. Reproduced from ref. 32 with permission from Elsevier B.V., copyright 2020.

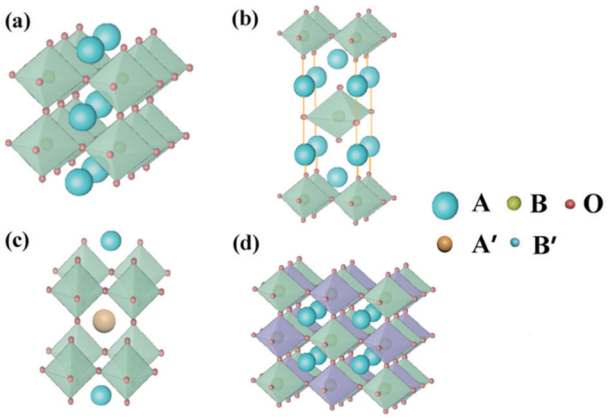

Fig. 3 Crystal structure of (a) the ideal ABO_3-type perovskite oxides, (b) Ruddlesden–Popper perovskite oxides ($(AO)(ABO_3)_n$), (c) A-site ordered double perovskite oxides ($AA'B_2O_6$) and (d) B-site ordered double perovskite oxides ($A_2BB'O_6$).

of O^{2-} can store twice charges in one charge/discharge cycle than Li^+ intercalation. Therefore, perovskite oxides have been regarded as tremendously promising candidate materials for SCs.

To date, some high-quality reviews on perovskite oxides for energy conversion and storage applications have been published.[36–39] However, there is still a lack of application and development of perovskite oxides in SCs. In this review, we first review the structure and composition of perovskite oxides. Secondly, perovskite oxides as electrode materials for SCs are introduced. Thirdly, the optimization strategies and applications of perovskite oxides in SCs are discussed. Finally, the application opportunities and challenges of perovskite oxides in SCs are presented.

2. Structure and composition of perovskite oxides

Perovskite oxides with the general formula of ABO_3, originating from $CaTiO_3$, are a family of oxides.[40] An ideal structure of perovskite oxides is shown in Fig. 3a. The A cation is located at the cube's body center, the B cation is at each of the eight corners, and O^{2-} is at each of the centers of the 12 edges. In this structure, twice the B–O bond distance is equal to a (a is the cubic unit cell parameter), and the A–O bond distance is equal to $a/2^{1/2}$.

In reality, it was found that the cubic structure was still retained in ABO_3 compounds, even though the bond length relationship between A–O and B–O does not strictly meet the above rule. To measure the ideal deviation, Goldschmidt introduced a tolerance factor (t), defined by the equation[41]

$$t = \frac{R_A + R_O}{\sqrt{2}(R_B + R_O)}$$

Here R_A, R_B, and R_O are the radii of A-site ions, B-site ions, and oxygen ions, respectively. Based on Shannon's ionic radii data,[35] t = 1 corresponds to an ideal cubic structure, and different distortions are observed as t decreases.[42] The perovskite oxide structure is stable when t is in the range from 0.75 to 1.00. Notably, in addition to the above ion radius rule, the other requirement that needs to be met for the perovskite structure is the principle of electrical neutrality: the sum of the charges of A- and B-site cations must be equal to the total of oxygen anions. Adding these constraints together, the perovskite oxide structure displaying incomparable flexibility can accommodate variable occupancy of different structural and electronic lattice defects.[43,44] For instance, partial substitution of A and B-site cations by doping with different cations with varying ionic radius and valence has been extensively adopted to tailor perovskite oxide properties in both physical and chemical terms, such as lattice structure, electronic structure, lattice defects, and diffusion behavior.[45,46]

In addition to the ABO_3-type perovskite, other oxides are also associated with perovskites, such as Ruddlesden–Popper (RP) perovskites ($(AO)(ABO_3)_n$, Fig. 3b),[47] A-site ordered double perovskite oxides ($AA'B_2O_6$, Fig. 3c),[48] and B-site ordered double perovskite oxides ($A_2BB'O_6$, Fig. 3d).[49] From the composition, about 90% of the metal elements in the periodic table can be the cations in ABO_3-type perovskite oxides.[50] The common elements are shown in Fig. 4. Generally, A-site metal's significant role is to elevate the thermodynamic stability, and the B-site metal regulates the electrochemical reactions. For the electrode material applications in SCs, alkaline-earth (such as Sr and Ba) and rare-earth metals (such as La and Sm) are the principal A-site cations, and the B-site cation is usually a transition metal (such as Mn, Co, and Ni).

3. Perovskite oxides as electrode materials for SCs

3.1 The single perovskite oxides

ABO_3 holds great promise as an active material for SCs due to its high tap density and oxygen vacancy concentration. In this

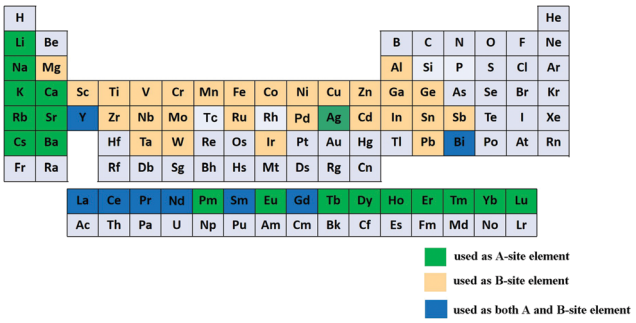

Fig. 4 Common elements in ABO_3-type perovskite oxides.

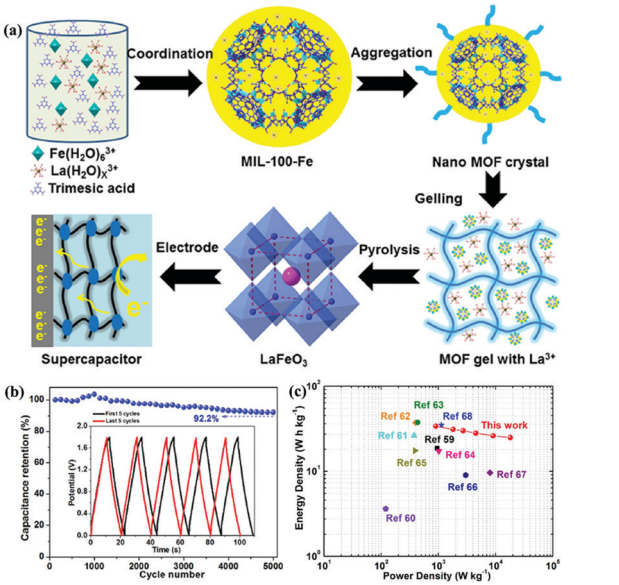

Fig. 5 (a) Schematic illustrations showing the synthesis of perovskite $LaFeO_3$. (b) Cycling stability *versus* cycle number graph, inset: the first and last five GCD cycles. (c) Ragone plots (energy density *vs.* power density) of this work and other devices. Reproduced from ref. 61 with permission from Elsevier B.V., copyright 2020.

section, perovskite oxides are divided into four categories, lanthanum-based, strontium-based, cerium-based, and other perovskite oxides, to review their application.

3.1.1 Lanthanum-based perovskite oxides. In recent years, lanthanum-based perovskite oxides have attracted great interest in SCs, due to their good thermal stability, facile synthesis, oxygen storage, low cost, and improved electrical conductivity.[51]

$LaMnO_3$ is the first lanthanum-based perovskite oxide to be applied in SCs. Because of the defective cation-deficient lattice and the presence of manganese in two oxidation states (Mn 3p/Mn 4p), $LaMnO_3$ shows a relatively stable and constant oxygen excess.[52] In 2014, a specific capacitance of about 609.8 F g^{-1} for $LaMnO_3$ was reported by Mefford *et al.*[31] $LaNiO_3$ is reported to exhibit a similar charge storage mechanism to $LaMnO_3$ but with lower electrical resistivity (about 10^{-4} Ω).[53–58] Shao *et al.*[59] developed a template-free solvothermal approach to fabricate a hollow spherical structure of $LaNiO_3$, showing a high specific capacitance (422 F g^{-1} at 1 A g^{-1}) and good cycle stability (83.3% capacitance retention after 5000 cycles).

Compared with $LaNiO_3$, $LaFeO_3$ is more stable because Fe^{3+} has a stable electronic configuration of $3d^5$.[60] Zhang *et al.*[61] reported mesoporous $LaFeO_3$ nanoparticles as the electrode material for SCs (Fig. 5a). A two-electrode symmetric SC cell (SSC) based on this material displayed a high energy density of 34 W h kg^{-1} at a power density of 900 W kg^{-1} with 92.2% capacitance retention after 5000 cycles (Fig. 5b and c). In Harikrishnan's work,[62] $LaCoO_3$ nanoparticles were prepared by the co-precipitation method. Because cobalt atoms have many oxidation states (2+, 3+, and 4+), $LaCoO_3$ exhibited good electrochemical redox properties with a specific capacitance of 299.64 F g^{-1} at 10 A g^{-1}. Recently, Hussain's group used the sol–gel method to synthesise a hierarchical mesoporous nanostructure of $LaCrO_3$. The obtained sample revealed superior specific capacitance (1268 F g^{-1} at 2 A g^{-1}) and good stability (91.5% capacitance retention after 5000 cycles).[63]

3.1.2 Strontium-based perovskite oxides. Strontium-based perovskite oxides have attracted substantial research attention as SC electrode materials because of their natural abundance, good ionic and electronic conductivity, and tolerance to reduction–oxidation cycling.[64]

The earliest application of strontium-based perovskite oxides in the field of SCs can be traced back to 1999.[65] Garche *et al.*[66] reported $SrRuO_3$ with a capacitance of 270 F g^{-1}. Other strontium-based perovskite oxides (such as $SrCoO_{2.5}$, $SrMnO_3$, and $SrTiO_3$) also show potential for SCs. Xiao *et al.*[67] used a conventional solid-state reaction route to synthesize the orthorhombic structure of $SrCoO_{2.5}$, and the resultant $SrCoO_{2.5}$ displayed a specific capacitance of 168.5 F g^{-1}. George *et al.*[68] fabricated $SrMnO_3$ nanofibers using sol–gel assisted electrospinning, which was followed by calcination at different temperatures (600 °C, 700 °C, and 800 °C). It was found that the nanofibers synthesized at 700 °C with small grains comprising a porous structure performed (321.7 F g^{-1} at 0.5 A g^{-1}) better than other samples. The high porosity and surface area are likely to improve the SC performance with more ion diffusion and adsorption in the charge–discharge process. Additionally, with high porosity, sufficient electrochemically active sites are exposed, which can hold a large quantity of the electrolyte, providing more electrode–electrolyte accessibility.[69] Similarly, Sharma *et al.*[70] demonstrated the charge storage properties of mesoporous $SrTiO_3$ (STO) with a cubic crystal structure. In their study, the Barrett-Joyner-Halenda (BJH) average pore diameter and pore volume of STO were tested as 15.18 nm and 0.249 cm^3 g^{-1}, respectively. Such pores provide a large number of active sites and low charge transfer resistance.[71] Consequently, STO displayed a high capacitance of 592 F g^{-1} at 5 mV s^{-1}. Interestingly, based on this material, a SSC was constructed, which exhibited maximum energy (27.8 W h kg^{-1}) and power density (1921 W kg^{-1}) with excellent cycling stability (99% capacitance retention after 5000 cycles).

3.1.3 Cerium-based perovskite oxides. Cerium-based perovskite oxides are attractive candidates due to their high dielectric constant, low cost, high bandgap, and variable valence states between Ce^{3+} and Ce^{4+}.[72,73] Their high SC performance in an

alkaline solution at room temperature has also been confirmed recently. In this context, Hu and coworkers utilized electrospinning and consequent calcination processes to synthesize $CeMnO_3$ nanofibers (NFs).[74] It is generally well accepted that A-site cations of perovskite oxides cannot contribute to the electronic structure near the Fermi level.[37] However, because cerium has high redox ability between Ce^{3+} and Ce^{4+}, the faradaic redox reaction (Ce^{4+}/Ce^{3+} and Mn^{3+}/Mn^{4}) occurred on the $CeMnO_3$ electrode surface. As a result, the specific capacitance of $CeMnO_3$ NFs was 159.59 F g^{-1} at a current density of 1 A g^{-1}. Very recently, other cerium-based perovskite oxides ($CeCoO_3$, $CeNiO_3$, and $CeCuO_3$) showed a specific capacitance of 128, 189, and 117 F g^{-1}, respectively.[75] Similarly, the capacitance of $CeBO_3$ (B = Co, Ni, Cu) perovskite oxides is ascribed to the redox reactions of Ce^{4+}/Ce^{3+} and $B^{m+}/B^{(m+1)+}$.

3.1.4 Other single perovskite oxides. In addition to the several types discussed above, other single perovskite oxides (such as $BiFeO_3$, $NiMnO_3$, $NiTiO_3$, and $CoTiO_3$) have also received attention recently.[76–81] Yin *et al.*[77] prepared $BiFeO_3$ nanoplates by a hydrothermal method. The obtained $BiFeO_3$ displayed a specific capacitance (254.6 F g^{-1}) that was almost 3.1 times higher than that of the electrochemically deposited counterpart.[78] Kim *et al.*[79] utilized the same approach to synthesize three-dimensional $NiMnO_3$. The prepared $NiMnO_3$ delivered a specific capacitance of 99.03 F g^{-1}. The cycling-stability test showed a decrease in capacitance retention after 7000 cycles (77% capacitance retention after 7000 cycles), which can be attributed to the loss of the transition metal oxide during the redox reaction. Beyond that, the metal titanate $MTiO_3$ (M = Ni, Co) has also been studied extensively as a SC material. In Kitchamsetti's work, mesoporous nickel titanate (NTO) rods were synthesized *via* the sol–gel method.[80] The obtained sample showed a good specific capacitance (542.26 F g^{-1}). Similarly, Kitchamsetti *et al.*[81] reported the highly porous $CoTiO_3$ (CTO) micro rods with high specific capacitance (608.4 F g^{-1}), specific power (4835.7 W kg^{-1}), and specific energy (9.77 W h kg^{-1}).

3.2 Optimization strategy of perovskite oxides

Because the oxygen vacancies can provide charge-storage sites, increasing the number of oxygen vacancies is an effective strategy to enhance capacitance. For perovskite oxides, the number of oxygen vacancies is highly dependent on their structure and composition. Therefore, well-designed perovskite oxides are critical for achieving high electrode performance. Moreover, composite materials generally have better properties than the individual components. In the following sections, we discuss two aspects to optimize the SC of perovskite oxides: creating oxygen vacancies and compositing with other materials.

3.2.1 Creating oxygen vacancies in perovskite oxides. The flexibility of the structure and composition of perovskite oxides presents a variety of defect structures. In this section, we discuss three ways of improving perovskite's oxygen vacancy concentration (modulating the stoichiometry of the anion or cation, A-site doping, and B-site doping) to affect the performance of SCs.

3.2.1.1 Modulating the stoichiometry of the anion or cation. The non-stoichiometry phenomenon in perovskite oxides is widespread, arising from either anion deficiency ($ABO_{3-\delta}$) or anion excess ($ABO_{3+\delta}$) or cation deficiency in the A/B-site.[82] Modulating the stoichiometry of the anion or cation to enhance electrochemical performance is crucial because it generates oxygen vacancies.[37]

Due to stability issues, there have been few studies on oxygen-excess perovskite $ABO_{3+\delta}$ with interstitial oxygen atoms.[83] However, oxygen-deficient perovskite oxides have been studied extensively. Typically, $ABO_{3-\delta}$ is prepared by post-processing methods, such as, thermal treatment of perovskite oxides at elevated temperatures under a low-oxygen partial pressure or inert or reducing atmosphere (such as nitrogen, argon, hydrogen, or their mixture, or a vacuum).[84–88] One typical example is that of Che *et al.*,[89] who fabricated two kinds of nonstoichiometric $LaNiO_{3-\delta}$ through the sol–gel method and further calcination at different temperatures (800 and 850 °C), which were named LNO and LNO-HT, respectively. In their experiment, the oxygen non-stoichiometry δ of LNO and LNO-HT was 0.37 and 0.27, respectively. They found that the specific capacitance of LNO increased by 75 F g^{-1} compared with LNO-TH. Interestingly, LNO showed cycling stability (94.5% capacitance retention after 15 000 cycles) superior to that of hollow spherical $LaNiO_3$.[56] $LaMnO_3$ suffers from similar limitations as other oxides, such as low conductivity and short cycle stability.[90] Elsiddig *et al.*[91] synthesized a series of $LaMn_{1\pm x}O_3$ by controlling Mn/La molar ratios (0.90, 0.95, 1, 1.05, and 1.1). Compared with the stoichiometric $LaMnO_3$ sample, significant differences were observed regarding Mn^{4+} ions and oxygen vacancies, which improve their conductivity and provide additional sites to accept more ions from the electrolyte and hence improve the electrochemical performance (Fig. 6a and b). In particular, $LaMn_{1.1}O_{3-\delta}$ showed the lowest equivalent series resistance (R_s = 3.5 Ω) and the best specific capacity (727.6 C g^{-1} at 1 A g^{-1}).

3.2.1.2 A-site doping. In general, the SC performance of perovskite oxides is closely related to the B-site transition metal

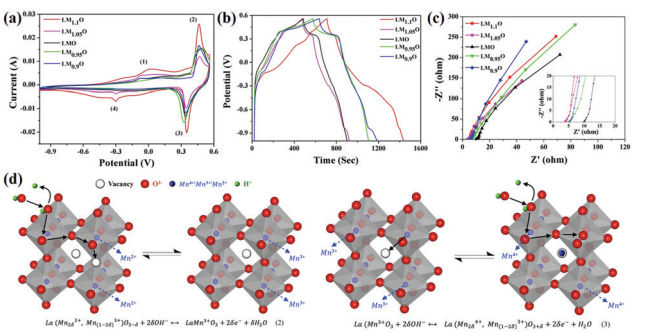

Fig. 6 (a) Cyclic performance of the $LM_{1\pm x}O_3$ samples at a scan rate of 0.01 V s^{-1}. (b) Charge–discharge curves in a potential window of −1 to 0.56 V at 1 A g^{-1}. (C) EIS of the $LM_{1\pm x}O_3$ samples with the inset of enlarged R_s at high frequencies. (d) Charge storage mechanism in $LM_{1\pm x}O_3$ perovskite oxide materials. Reproduced from ref. 91 with permission from Elsevier B.V., copyright 2017.

element. The A-site element (such as lanthanide and alkaline earth element) is inert for the redox reaction directly. However, the A-site cation may affect the electronic structure and coordination. Partial substitution of the A-site by a low-valence cation (such as Sr^{2+} and Ca^{2+}) generates addition oxygen vacancies and shifts a large proportion of the B-site transition-metal ions to unstable oxidation states ($B^{m+}/B^{(m+1)+}$ redox couple).[92] As a result, electronic conductivity is increased, and electrochemical performance is enhanced.

Since the alkaline earth metals and rare earth metals share similar atomic radius, it is energetically favorable for the former to substitute the latter.[38] In this direction, Mo *et al.*[93] prepared Ca-doped perovskite lanthanum manganates ($La_{0.5}Ca_{0.5}MnO_3$) by a sol–gel method. The specific capacitance of $La_{0.5}Ca_{0.5}MnO_3$ was 2.4 times that of pure $LaMnO_3$ (72 F g^{-1}). Similarly, Wang *et al.*[94] doped $LaMnO_3$ with Sr and reported that its capacitance was slightly increased from 187 to 198 F g^{-1} at 0.5 A g^{-1}, and the cycle life was enhanced from 40% to 80% after 1000 cycles. To gain more insight into the influence of the substitution degree on electrochemical performance, Tian's group synthesized $La_{1-x}Sr_xMnO_3$ (x = 0, 0.15, 0.3, 0.5) by the sol–gel method.[95] It was observed that the aggregation degree of nanoparticles, specific capacitance, and charge transfer resistance are affected by the value of x. In particular, when x = 0.15 ($La_{0.85}Sr_{0.15}MnO_3$), the lowest R_{ct} (1.6 Ω) and the best specific capacitance (102 F g^{-1}) were observed. Furthermore, the ASCs employing $La_{0.85}Sr_{0.15}MnO_3$ as the anode material and AC as the cathode material reached an energy density of 3.6 W h kg^{-1} at a low power density of 120 W kg^{-1}. Recently, Alexander and coworkers synthesized a series of perovskite oxides with the composition $La_{1-x}Sr_xBO_{3-\delta}$ (x = 0–1; B = Fe, Mn, Co) to study anion-based PCs systematically.[96] They found that more significant oxygen vacancy content upon systematic incorporation of Sr^{2+} linearly increases the surface-normalized capacity with a slope controlled by the B-site element. Moreover, $La_{0.2}Sr_{0.8}MnO_{2.7}$ exhibited the best specific capacitance (492 A g^{-1}) relative to the Fe and Co oxides. The formation energy of oxygen vacancies due to aliovalent substitution depends on the alkaline-earth metals.[97] The influence of Ba and Ca doping on the SC of $SrMnO_3$ nanofibers was studied by Luo *et al.*[68] Doping 20 mol% Ba to the $SrMnO_3$ matrix significantly enhanced the specific capacitance from 321.7 F g^{-1} to up to 446.8 F g^{-1}. Moreover, the ASC fabricated using $Sr_{0.8}Ba_{0.2}MnO_3$ showed an energy density of 37.3 W h kg^{-1} at a power density of 400 W kg^{-1} and a superior capacitance retention of 87% after 5000 cycles.

3.2.1.3 B-site doping. The charge storage mechanism embraces electrochemical reactions. Incorporating oxygen ions into the vacancies requires a simultaneous change in the B cation's oxidation state. B-site doping is another effective measure to enhance electrical performance because it can produce oxygen vacancies and improve the crystal structure's stability.[98]

Cobalt-based perovskite oxides are superior to Mn-based ones due to their larger oxygen vacancy concentration and higher oxygen-ion mobility.[99] However, some cobalt-based perovskite oxides (such as cubic phase $SrCoO_{3-\delta}$) are not stable at room temperature. To widely implement cobalt-based perovskite oxides application in SCs, Sharma and coworkers doped Mo to substitute Co in $SrCoO_{3-\delta}$ partially (Fig. 7a).[100] It was found that the oxygen vacancies of $SrCo_{0.9}Mo_{0.1}O_3$ (SCM) were 2.1 times greater than that of $SrCoO_{3-\delta}$. Additionally, SCM's specific capacitance (1223.34 F g^{-1} at 1 A g^{-1}) was increased by 1.36 times that of $SrCoO_{3-\delta}$ (Fig. 7b). Notably, the ASC constructed by using lacey reduced graphene oxide nanoribbon (LRGONR) as a negative electrode showed long-term stability (165.1% activated specific capacitance retention after 10 000 cycles) (Fig. 7c). Most importantly, it also achieved a specific energy density of 74.8 W h kg^{-1} at a power density of 734.5 W kg^{-1} (Fig. 7d). Similarly, Nb-doped $SrCoO_{3-\delta}$ with a gravimetric capacitance of *ca.* 773.6 F g^{-1} (2034.6 F cm^{-3}) and great cycling stability (95.7% capacitance retention after 3000 cycles) was reported by Shao *et al.*[101] Furthermore, an ASC was assembled using $SrCo_{0.9}Nb_{0.1}O_{3-\delta}$ (SCN) and AC as the cathode and anode. The device possessed an energy density of 37.6 W h kg^{-1} at a power density of 433.9 W kg^{-1}, and it still maintained an energy density of 32.9 W h kg^{-1} at a higher power density of 9864.2 W kg^{-1}. Also, it displayed long-duration cycling performance (about 1.7% loss after 5000 cycles). The B-site doping can also affect the potential window of perovskite oxides. Garche's team studied the influence of B site element doping on the stability window of $SrRuO_3$. Interestingly, 20 mol% Mg doping was found to increase the specific capacitance of $SrRuO_3$ without changing its stability window.[66] In contrast, Fe or Co substitution could lead to a decreased stability window.

3.2.2 Perovskite oxide composites. Based on previous work, the defective structure of perovskite oxides and excellent oxygen ion mobility can boost the conversion of B^{x+} to a high

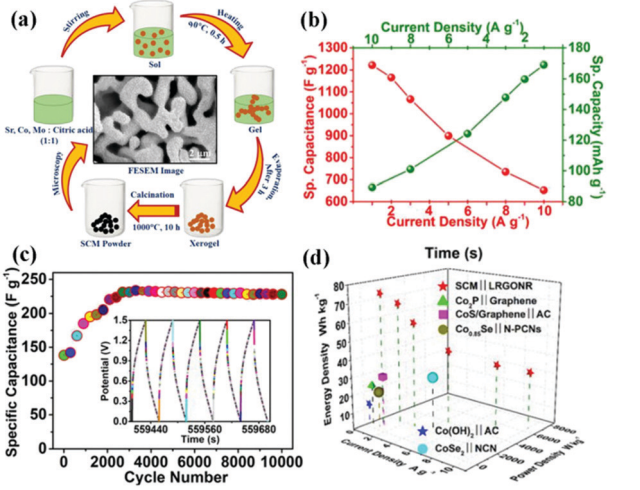

Fig. 7 (a) Schematic illustration of the synthesis of SCM. (b) Electrochemical performance of the SCM electrode evaluated through GCD at different current densities. (c) Cycling stability of the ASC at 10 A g^{-1}. The inset shows the last five GCD cycles. (d) Ragone plot of a hybrid SCM cell compared to literature reports. Reproduced from ref. 100 with permission from WILEY-VCH Verlag GmbH & Co. KGaA, Weinheim, copyright 2018.

valence state, thus obtaining superior electrochemical properties. Despite this, the drawbacks of perovskite oxides, including the low surface area and high transport resistance of aggregated nanoparticles, hinder the further improvement of electrochemical performance. An effective strategy to address these problems is to combine ABO_3 with other materials (such as noble metals, metal oxides, and carbon materials), forming composites with enriched chemistry.

3.2.2.1 Perovskite oxides/noble metals. Noble metals, including gold (Au) and platinum (Pt) group metals with good electric conductivity, can facilitate the transport of electrons that arise from the oxidation/reduction of PCs to the current collectors.[102] Nevertheless, owing to the scarcity and high cost of noble metals, their integration with other sustainable and cheap materials is considered one of the most attractive strategies to minimize their consumption. Perovskite oxides possess characteristics of natural abundance and low cost. Unfortunately, the electrical conductivity of perovskite oxides is still not satisfactory. Therefore, combining perovskite oxides with noble metals is expected to improve their SC performance by creating synergistic effects.

Ag has the highest conductivity among the noble metals. Besides, it also has the advantage of reasonable cost and has an acceptable activity.[103] Lang *et al.*[104] reported that Ag nanoparticle decorated $La_{0.85}Sr_{0.15}MnO_3$ was designed and used as an electrode for SCs. Since Ag has much higher electrical conductivity than that of carbon materials, it could build electron transfer channels. Additionally, the redox reaction between Ag and Ag_2O in an alkaline electrolyte solution could contribute a small amount of pseudocapacitance. As a result, the Ag@LSM15 composite delivered a high specific capacitance (186 F g^{-1} at 1 A g^{-1}) and a long cycle life (100% capacitance retention after 1000 cycles). Moreover, based on this material, the ASC was constructed, showing a maximum energy density of 20.6 W h kg^{-1} at a power density of 1700 W kg^{-1}. In another study, Ag nanoparticles were grown directly on a porous perovskite $La_{0.7}Sr_{0.3}CoO_{3-\delta}$ (LSC) substrate (Ag/LSC) (Fig. 8a).[105] The effect of different mass loading of Ag (10.61, 30.60, and 51.31 mg) on performance was studied. The porous structure of LSC was preserved, and the surface became rough when the content of Ag was 30 mg (30 Ag/LSC) or less. This favorable structure can provide more active surface sites and facilitate rapid mass transport. Besides, the Ag/LSC electrode with 30 mg Ag loading also displayed lower R_s (1.28 Ω cm^2) and R_{ct} (0.61 Ω cm^2), giving rise to the best performance (14.8 F cm^{-2}) (Fig. 8b). Besides, an ASC based on 30 Ag/LSC as the negative electrode and carbon cloth (CC) as the positive electrode was constructed, displaying an energy density of 21.9 mW h cm^{-3} and a power density of 90.1 mW cm^{-3} at 5 mA cm^{-2} (Fig. 8c). Visibly, two ASCs in series were used to light an LED blue for 15 min after charged for 0.5 min at 50 mA cm^{-2} (Fig. 8c).

3.2.2.2 Perovskite oxides/metal oxides. Metal oxides have received more and more attention because their multiple numbers of oxidation states allow for up to an order of magnitude more generous energy storage compared to

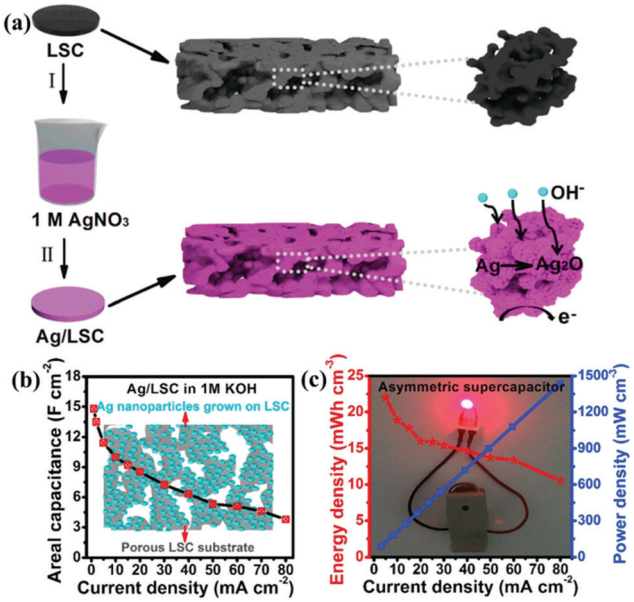

Fig. 8 (a) Schematic illustration of the preparation of Ag nanoparticles grown on a LSC substrate. (b) The areal capacitance of 30 Ag/LSC. (c) Electrochemical measurements of the asymmetric supercapacitor: Ragone plot at different current densities (inset: an LED bulb lighted by two asymmetric cells in series). Reproduced from ref. 105 with permission from Elsevier B.V., copyright 2017.

carbon-based EDLCs.[12] However, most metal oxides suffer from low conductivity, poor rate capability, and poor durability during charge/discharge processes. In contrast, perovskite oxides possess a stable structure and can produce much higher oxygen ion/electron conductivity and better surface oxygen exchange kinetics.[106] Hence, the composites of perovskite oxides and metal oxides are attractive alternatives because of their low cost in addition to the possibility to achieve high specific capacitance/capacity values and superb stability.

Among the metal oxides, MnO_2 stands out due to its high theoretical specific capacitance (about 1370 F g^{-1}), low cost, and natural abundance.[107,108] Lv *et al.*[109] synthesized $(La_{0.75}Sr_{0.25})_{0.95}MnO_{3-\delta}$ ((LSM)/MnO_2) composite as an electrode for SCs *via* a hydrothermal method. The resultant sample exhibited a larger specific capacitance (437.2 F g^{-1} at 2 mV s^{-1}). Compared with MnO_2, CeO_2 has low theoretical capacitance, but it has unique chemical properties. That is, it can be easily oxidized and reduced during the oxidation–reduction process.[110,111] Nagamuthu and co-workers reported $LaMnO_3$ mixed CeO_2 (CeO_2/$LaMnO_3$) nanocomposites with a higher specific capacitance (262 F g^{-1} at 1 A g^{-1}) in 1 M Na_2SO_4 solution.[112] Interestingly, they found that the CeO_2/$LaMnO_3$ nanocomposite was more suited for ASC negative electrodes. More specifically, an ASC device was assembled using the CeO_2/$LaMnO_3$ nanocomposites as the negative electrode and AC as the positive electrode, revealing an energy density of 17.2 W h kg^{-1} at a power density of 1015 W kg^{-1}. It is well established that the energy density (E) is proportional to the potential window (V). Thus, another way to elevate the energy density is to enlarge the potential window. A $La_{0.8}Sr_{0.15}MnO_3$@$NiCo_2O_4$

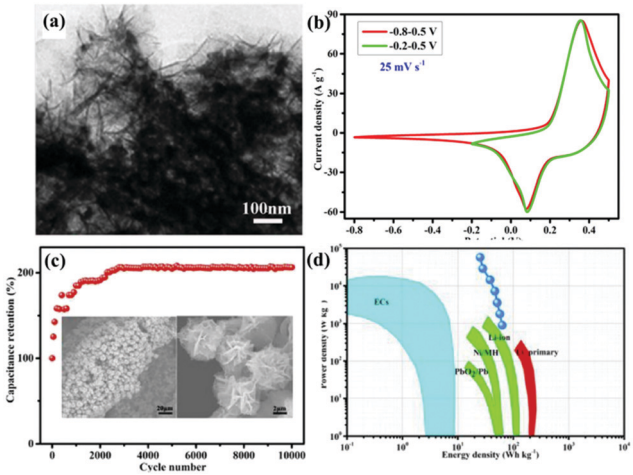

Fig. 9 (a) TEM images of LSM15@NC scratched down from the Ni foam. (b) Comparative CV curves at a scan rate of 25 mV s^{-1} within different potential windows of −0.8 to 0.5 V and −0.2 to 0.5 V. (c) Cycling performance (the insets show the morphology of LSM15@NC after 10 000 cycles). (d) Ragone plot. Reproduced from ref. 113 with permission from Elsevier B.V., copyright 2018.

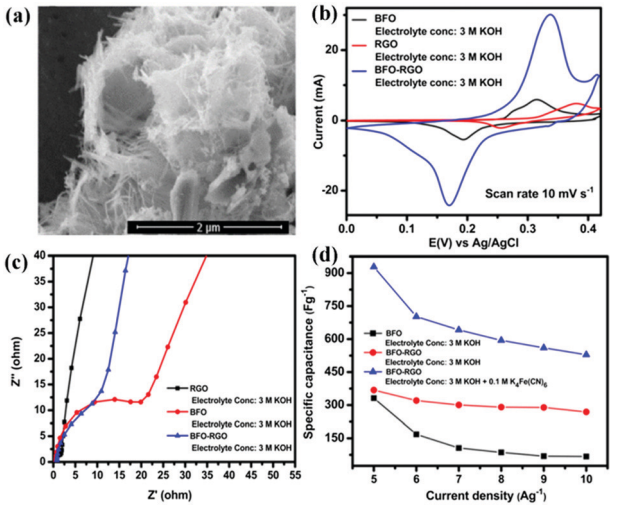

Fig. 10 FESEM micrographs of (a) BFO. (b) Cyclic voltammetry curves of BFO, RGO, and BFO–RGO electrodes at a scan rate of 10 mV s^{-1} in a 3 M KOH electrolyte. (c) Electrochemical impedance spectra of RGO, BFO, and BFO–RGO electrodes in a 3 M KOH electrolyte. (d) Change of the specific capacitance of BFO and BFO–RGO electrodes with changing current density from 5 to 10 A g^{-1}. Reproduced from ref. 117 with permission from American Chemical Society, copyright 2018.

(LSM15@NC) core–shell nanoflower structure directly grown on Ni foam (Fig. 9a) was constructed by Lang *et al.*[113] LSM15@NC showed a wide window and the coexistence of PC as well as EDLC behavior (Fig. 9b). Benefitting from the unique structure acting as a buffer for the volume change during the long-term charge–discharge tests, the specific capacitance of LSM15@NC was twice as much as that of the first cycle after 10 000 cycles (Fig. 9c). Moreover, the ASC using AC as the negative electrode and the LSM15@NC composite as the positive electrode delivered an energy density of 63.5 W h kg^{-1} at a power density of 900 W kg^{-1} (Fig. 9d).

3.2.2.3 Perovskite oxides/carbon materials. It is well known that carbonaceous materials (such as AC, graphene, graphene oxide, and reduced graphene oxide) with large specific surface area, good electronic conductivity, and high chemical stability have been widely applied in SCs.[114] The low intrinsic conductivity of perovskite oxides is the main drawback that limits their further application in SCs. The addition of carbonaceous materials to form perovskite oxides/carbon composites is an effective strategy to remedy this deficiency.

Due to the extra-large theoretical specific surface area (2630 m^2 g^{-1}) and superior electrical conductivity (6000 S cm^{-1}), graphene is usually added into perovskite oxides to enhance SC performance.[114,115] Graphene can effectively restrain the agglomeration of perovskite oxides. Meanwhile, it can provide a high-speed electron transport channel.[116] In return, the loading perovskite oxide nanoparticles are also available to maintain the structural nature of monolayer graphene for their function of increasing the distance between the graphene sheets.[116] Fig. 10a shows $BiFeO_3$ (BFO) nanowires immobilized on nanometer-thin RGO.[117] Based on this material, the specific capacitance (368.28 F g^{-1}) and charge transfer resistance are found to be superior to those of BFO and RGO (Fig. 10b and c). Notably, the electrolyte also has a more significant impact on the performance of BFO–RGO (Fig. 10d). To investigate the capacitive behavior of graphene–perovskite oxide compound materials in aqueous electrolytes of various acidity or basicity, Ataa *et al.*[118] tested reduced graphene performance sheets decorated $SrRuO_3$ (SRGO) in different electrolytes (1.0 M $NaNO_3$, 1.0 M H_3PO_4, and 1.0 M KOH). The SRGO exhibited the largest capacitance (160 F g^{-1}) in 1.0 M KOH.

As stated above, the electrochemical performance is enhanced compared with pure perovskite oxides after carbon introduction. The redox reaction of oxygenated groups on carbon nanostructures' surface contribute to pseudocapacitance.[119] In this regard, introducing surface functional groups or heteroatoms on the surface of carbon materials appears to be an effective way of improving the composite electrode's capacitance.[120,121] Elsiddig *et al.*[122] introduced a heteroatom to reduced graphene oxide (rGO) by substituting the hydroxyl groups with the nitrogen atoms. Then, the as-prepared nitrogen-doped graphene (N-rGO) sheets can be directly integrated with $LaMnO_3$ (LMO) through electrostatic interactions to form a three-dimensional network (LMO/N-rGO). Compared with pristine graphene and LMO, the obtained nanocomposites displayed the best specific capacitance (687 F g^{-1} at 5 mV s^{-1}) and stability (79% capacitance retention after 2000 cycles at 10 A g^{-1}). In another study, Shafi *et al.*[123] synthesized a composite material containing $LaMnO_3$, RGO, and polyaniline (PANI) by *in situ* chemical polymerization. Since the RGO support and PANI coating again provided good structural stability and good electrical conductivity, the synthesized ternary composite exhibited a specific capacitance of 802 F g^{-1} at 1 A g^{-1}. More importantly, the ASC with RGO as the negative electrode and ternary nanocomposite as the positive electrode exhibited a maximum energy density of 50 W h kg^{-1} at a power density of

2.25 kW kg^{-1}, with admirable long-term stability (117% capacitance retention after 100 000 cycles).

4. Derivative perovskite oxides

Some derivative perovskite oxides were reported to possess fast oxygen ion diffusion channels, in which the oxygen diffusion exhibited shallow activation energy.[124,125] Additionally, the oxygen-ion conductivity of some derivative perovskite oxides is even higher than that of many benchmark ABO_3.[45,126] Moreover, many derivative perovskite oxides also can present high concentrations of variable oxygen vacancies. In this context, derivative perovskite oxides have some potential for application in SCs, as shown in Table 1.

4.1 Double perovskite oxides

In 1951, double perovskite oxides were first discovered by Steward and Rooksby, expressed by the general formula of AA'BB'O_6, a derivative of ABO_3, extending the pristine framework to a super-lattice.[127] To date, double perovskite oxides have been widely investigated, because they have high oxygen surface exchange kinetics and fast oxygen ion diffusion rates, and good mixed ionic and electronic conductivity at elevated temperature. Compared with element-doped perovskite oxides, AA'BB'O_6 holds a more orderly structure arrangement, thereby preventing lattice distortion and improving cycling stability.

In general, cations are disordered and distributed homogeneously inside the AA'BB'O_6 lattice. Nevertheless, in some situations, cation ordering could occur (such as AA'B_2O_6 and A_2BB'O_6). It is worth mentioning that cation ordering could display better physical and chemical properties. Kumar's team reported the electrochemical performance of R_2MMnO_6 (R = La, Gd; M = Zn, Cu, Ni) perovskite oxides including La_2ZnMnO_6, La_2CuMnO_6, and Gd_2NiMnO_6, which showed a specific capacitance of 718.6 F g^{-1}, 205.5 F g^{-1}, 400.46 F g^{-1}, respectively, at different current densities.[128–130] To improve the SC properties, increasing the specific surface area and improving the nanoscale charge transport are useful measures. Meng and coworkers fabricated a hollow spherical porous structure of La_2CoMnO_6 by template impregnation (HS-LCMO).[131] For comparison, La_2CoMnO_6 was also prepared by the sol–gel method (SG-LCMO). The specific surface area of HS-LCMO and SG-LCMO was estimated to be 22.14 and 10.36 m^2 g^{-1}, respectively. Owing to its large specific surface area, HS-LCMO

Table 1 Applications and performances of different perovskite oxides in supercapacitors

Perovskite oxides	Methods	Structure	Electrolyte	Potential window	Capacitance	Ref.
$LaMnO_{2.97}$	Reverse-phase hydrolysis approach	Nanoparticles	1 M KOH	−1.2 to 0.0 V	609.8 F g^{-1} at 2 mV s^{-1}	31
$LaMn_{1.1}O_3$	Sol–gel method	Mesoporous	1 M KOH	−1.0 to 0.56 V	727.6 C g^{-1} at 1 A g^{-1}	90
$LaNiO_3$	Template-free solvothermal method	Hollow spheres	6 M KOH	0.0–0.45 V	422 F g^{-1} at 1 A g^{-1}	59
$LaNiO_{2.63}$	Sol–gel method	Nanoparticles	1 M KOH	0.2–0.6 V	478.7 F g^{-1} at 0.1 mV s^{-1}	89
$LaCoO_3$	Co-precipitation method	Nanoparticles	3 M KOH	0.0–0.5 V	299.64 F g^{-1} at 10 A g^{-1}	62
$LaCrO_3$	Sol–gel method	Hierarchical mesoporous	1 M LiCl	0.0–1.0 V	1268 F g^{-1} at 2 A g^{-1}	63
$BiFeO_3$	Hydrothermal method	Nanoplates	1 M NaOH	0.0–0.5 V	254.6 F g^{-1} at 1 mV s^{-1}	77
$LaFeO_3$	The MOF gel method	Mesoporous	1 M Na_2SO_4	−1.0 to 0.0 V	241.3 F g^{-1} at 1 A g^{-1}	61
$SrRuO_3$	Pyrolysis route	Porous	6 M KOH	−0.9 to 0.3 V	270 F g^{-1} at 20 mV s^{-1}	66
$SrTiO_3$	Sol–gel method	Mesoporous	3 M KOH	−0.2 to 0.6 V	592 F g^{-1} at 5 mV s^{-1}	70
$CeMnO_3$	Electrospinning	Nanofibers	6 M KOH	−0.1 to 0.6 V	155 F g^{-1} at 1 A g^{-1}	74
$CeCoO_3$	Electrospinning	Nanofibers	6 M KOH	−0.1 to 0.6 V	128 F g^{-1} at 0.5 A g^{-1}	75
$CeNiO_3$	Electrospinning	Nanofibers	6 M KOH	−0.1 to 0.65 V	189 F g^{-1} at 0.5 A g^{-1}	75
$CeCuO_3$	Electrospinning	Nanofibers	6 M KOH	−0.1 to 0.7 V	117 F g^{-1} at 0.5 A g^{-1}	75
$NiTiO_3$	Sol–gel method	Rod-like	2 M KOH	0.0–0.6 V	542.26 F g^{-1} at 1 A g^{-1}	80
$NiMnO_3$	Hydrothermal method	Three-dimensional hierarchical	6 M KOH	0.0–0.9 V	99.03 F g^{-1} at 100 mV s^{-1}	79
$CoTiO_3$	Sol–gel method	Mesoporous microrods	2 M KOH	0.0–0.6 V	608.4 F g^{-1} at 5 mV s^{-1}	81
$La_{0.85}Sr_{0.15}MnO_3$	Sol–gel method	Sphere	1 M KOH	−0.96 to 0.65 V	198 F g^{-1} at 0.5 A g^{-1}	94
$La_{0.5}Ca_{0.5}MnO_3$	Sol–gel method	Nanoparticles	1 M KOH	−1.0 to 0.6 V	170 F g^{-1} at 1 A g^{-1}	93
$Sr_{0.8}Ba_{0.2}MnO_3$	Sol–gel and electrospinning	Nanofibers	1 M Na_2SO_4	0.0–0.8 V	446.8 F g^{-1} at 0.5 A g^{-1}	68
$SrCo_{0.9}Mo_{0.1}O_3$	Sol–gel method	Nanoparticles	6 M KOH	−0.1 to 0.5 V	1223.34 F g^{-1} at 1 A g^{-1}	100
$SrCo_{0.9}Nb_{0.1}O_3$	Solid-state	Nanoparticles	1 M KOH	0.0–0.5 V	773.6 F g^{-1} at 0.5 A g^{-1}	101
La_2ZnMnO_6	Hydrothermal route	Nanoflakes	2 M KOH	0.0–0.6 V	718.6 F g^{-1} at 1 mV s^{-1}	128
La_2CuMnO_6	Hydrothermal route	Nanoparticles	2 M KOH	0.0–0.45 V	205.5 F g^{-1} at 0.5 A g^{-1}	129
Gd_2NiMnO_6	Wet chemical route	Nanoparticles	4 M KOH	0.2–0.6 V	400.46 F g^{-1} at 1 A g^{-1}	130
La_2CoMnO_6	Template impregnation method	Hollow spheres	1 M Na_2SO_4	−0.1 to 1.0 V	376 F g^{-1} at 1 A g^{-1}	131
Y_2NiMnO_6	Hydrothermal route	Nanowires	0.5 M KOH	0.2–0.5 V	77.76 F g^{-1} at 30 mA g^{-1}	132
$PrBaMn_2O_{6-\delta}$	Sol–gel method	Nanoparticles	6 M KOH	0.0–0.5 V	1034.8 F g^{-1} at 1 A g^{-1}	133
$PrBaCo_2O_{5+\delta}$	Sol–gel method	Nanoparticles	1 M KOH	−0.1 to 0.55 V	428.2 C g^{-1} at 1 mV s^{-1}	136
$Ba_2Bi_{0.1}Sc_{0.2}Co_{1.7}O_{6-\delta}$	Sol–gel method	Nanoparticles	6 M KOH	0.0–0.6 V	796.7 F g^{-1} at 1 A g^{-1}	137
$Sr_2CoMoO_{6-\delta}$	Sol–gel method	Spherical particles	6 M KOH	−0.1 to 0.4 V	747 F g^{-1} at 1 A g^{-1}	138
$La_2NiO_{4+\delta}$	Citrate method	Porous	3 M KOH	0.0–0.6 V	657.4 F g^{-1} at 2 mV s^{-1}	141

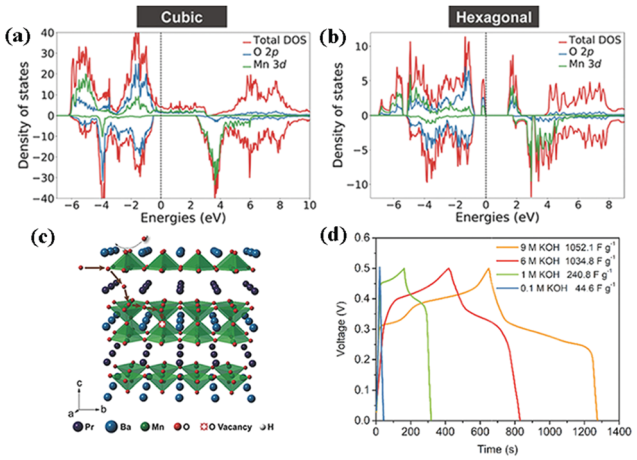

Fig. 11 DFT+U calculated density of states (DOS) for (a) cubic and (b) hexagonal PBM. (c) A schematic diagram of oxygen intercalation into r-PBM during the energy storage process. (d) Galvanostatic charge–discharge profiles of r-PBM. Reproduced from ref. 133 with permission from WILEY-VCH Verlag GmbH & Co. KGaA, Weinheim, copyright 2018.

displayed a specific capacitance (376 F g^{-1}) which was 4 times that of SG-LCMO (94 F g^{-1}). Similarly, Y_2NiMnO_6 nanowires (NWs) were prepared by a hydrothermal route. The resultant Y_2NiMnO_6 NWs exhibited a specific capacitance (77.76 F g^{-1}) which was higher than that of the counterparts prepared by the sol–gel method.[132] The crystal structure of perovskite oxides is closely related to the calcination temperature. Shao's team demonstrated that the reduction of $PrBaMn_2O_{6-\delta}$ (r-PBM) in a hydrogen atmosphere at 850 °C led to a phase transition from a mixed hexagonal and cubic phase to a cubic phase PBM (Fig. 11a and b).[133] Based on density functional theory (DFT) calculations, it is somewhat easier to form an oxygen vacancy in cubic PBM than in the hexagonal phase. Correspondingly, the formation of a layered double perovskite oxide structure after hydrogen reduction (800 °C for 45 min) significantly increased the oxygen vacancy concentration and oxygen anion diffusion rate, thus contributing to the capacitance (Fig. 11c). Notably, the r-PBM with a low specific surface area (7.83 m^2 g^{-1}) exhibited a gravimetric capacitance of 1034.8 F g^{-1} (Fig. 11d).

To further explore the effect of cation ordering on the performance of SCs, more effort has been made.[134,135] Wang *et al.*[136] synthesized A-site cation-ordered double perovskite oxide $PrBaCo_2O_{5+\delta}$ (PBCO) by the sol–gel method. They found that oxygen atoms located in the Pr^{3+} planes can be partially or even entirely removed, producing numerous oxygen vacancies in the perovskite oxide structure. Accordingly, the synthesized PBCO showed a good specific capacity (428.2 C g^{-1}). Notably, PBCO displayed cycling stability (93% capacitance retention after 2000 cycles at 10 A g^{-1}) superior to that of some single perovskite oxides (such as $BiFeO_3$ and $LaMnO_3$).[77,91] Beyond that, Xu *et al.*[137] reported that B-site cation-ordered double perovskite oxide $Ba_2Bi_{0.1}Sc_{0.2}Co_{1.7}O_{6-\delta}$ (BBSC) was a good anion-intercalation-type electrode for SCs. For comparison, the oxygen vacancy-disordered $Ba_{0.5}Sr_{0.5}Co_{0.8}Fe_{0.2}O_{3-\delta}$ (BSCF) electrode was also studied. It was found that the oxygen vacancy density of BBSC is larger than that of BSCF, and the simultaneous leaching of Ba from the A site and Bi from the B site of BBSC could minimize the cation deficiency in BBSC. As a result, BBSC delivered a specific capacitance (1050 F g^{-1}) higher than that of BSCF. Hence, the ASC fabricated using BBSC displayed an energy density of 70 W h kg^{-1} at a power density of 787 W h kg^{-1}. $Sr_2CoMoO_{6-\delta}$ (DP-SCM) as an intercalation PC was reported by Tomar *et al.*[138] In their study, B site-ordering was based on the difference between oxidation states of Co and Mo (greater than 2) with a large ionic radii difference. It was found that the synergy of Co/Mo has good redox ability, further facilitating high oxygen mobility, resulting in DP-SCM achieving a specific capacitance of 747 F g^{-1} at 1 A g^{-1} with a rate capability of 56% up to 10 A g^{-1}.

4.2 Ruddlesden–Popper oxides

RP perovskite oxides were first studied in 1958 by Ruddlesden and Popper.[139] Alternating perovskite $(ABO_3)^-$ and rock-salt $(AO)^+$ layers in the homologous series of titanates ($Sr_{n+1}TinO_{3n+1}$) were discovered.[140] The unique layered structure allows two sorts of oxygen species (oxygen vacancy, interstitial oxygen). The oxygen vacancy exists in the perovskite layer, while the interstitial oxygen is found in the rock-salt layer. Compared with ABO_3-type, RP perovskite oxides show superior mixed ionic and electronic conductivity. Sang *et al.*[141] prepared RP-type perovskite oxide $La_2NiO_{4+\delta}$ *via* a citrate method and used it as the active material for SCs. It was found that there are two ways of oxygen extrusion and only one way of oxygen insertion in $La_2NiO_{4+\delta}$. Interestingly, $La_2NiO_{4+\delta}$ showed a high specific capacitance of 657.4 F g^{-1} at a scan rate of 2 mV s^{-1}, which was better than the capacitance of $LaMnO_3$ (609.8 F g^{-1}).[31] Recently, to optimize the surface properties of RP particles, Wei and coworkers synthesized $La_2NiO_{4+\delta}$ coated with Ag ($La_2NiO_{4+\delta}$@Ag).[142] Because of the unique layered structure of $La_2NiO_{4+\delta}$ and the quick reversible redox process of Ag/AgO_2, the $La_2NiO_{4+\delta}$@Ag electrode showed better anion intercalation performance compared to $La_2NiO_{4+\delta}$, such as large capacity (466.4 C g^{-1} at 1 mV s^{-1}) and good cycling stability (average efficiency approximated 93% in 10 000 cycles). Furthermore, a hybrid SC device assembled using $La_2NiO_{4+\delta}$@Ag and AC as the cathode and the anode showed a high energy density of 44.7 W h kg^{-1} at a power density of 800 W h kg^{-1}.

5. Conclusions and outlooks

With the unique structure, compositional flexibility, and inherent oxygen vacancy, perovskite oxides have recently been widely employed as electrode materials for SCs. Notably, as an active material of intercalation-type capacitors, perovskite oxides are characterized by high oxygen vacancy concentrations and do not require high surface area to achieve a high energy storage capacity. This article mainly summarizes the recent advances in perovskite oxides (*i.e.*, single, double, and RP perovskite oxides) for SCs. Further improvement of perovskite oxides' electrochemical properties by increasing oxygen vacancy concentration

and constructing composites is discussed. Despite many efforts in this field, several aspects still need to be considered in the design of perovskite oxide electrode materials in the future.

(1) During the charge storage process, the valence state change of the B-site cation with a low energy barrier in perovskite oxides is preferred.[137] To date, Mn, Ni, Fe, and Co have been studied as B site elements. Some early transition metals, such as Ti, Zr, V, and Nb, share similar ionization energies and ionization energy differences with Mn,[143] which is expected to be the B site element of perovskite oxide electrodes.

(2) B-site substitution by a metal element has been proven as a feasible approach to create oxygen vacancies in perovskite oxides, thereby boosting their performance as SC electrode materials.[100,101] In contrast, non-metal doping at the B-site was shown to improve the phase stability, electrical conductivity, and oxygen vacancies of perovskite oxides.[144–146] Therefore, more research work on non-metal doping at the B-site is expected in this field.

(3) The electronic conductivity of RP perovskite oxides is anticipated to increase as their n value increases.[147] However, most of the reports are on RP perovskite oxides with $n = 1$. RP perovskite oxides with higher n values as advanced SC electrode materials are therefore expected.

(4) The morphology of perovskite oxides plays a crucial role in boosting electrochemical performance. However, perovskite oxides generally are synthesized at high temperatures above 600 °C, leading to limited low surface areas ($<10\ m^2\ g^{-1}$) and less exposure to active sites.[148] Therefore, controllable synthesis of nanostructures (such as hollow, core–shell, and nanoarray) with large specific surface area and high redox activity is vital for achieving high energy/power densities of perovskite oxide SC electrodes.

(5) Apart from the architecture and electronic configurations, electrolytes also optimize perovskite oxides' energy-storage performance. Aqueous electrolytes like KOH with a narrow working voltage range of ~1.23 V and Na_2SO_4 (~2 V) are by far the most investigated media. The utilization of organic (2.5–3.5 V) or ionic liquid electrolytes (2–6 V) offers a wide voltage window, further improving the energy density. Notably, the introduction of additional redox-active compounds such as $CuCl_2$, $KMnO_4$, KI, KBr, Na_2MoO_4, and $K_3Fe(CN)_6$, *i.e.*, the formation of a redox electrolyte, can further improve the electrode materials' electrochemical performance. For instance, an additional 0.1 M $K_4[Fe(CN)_6]$ in 3 M KOH causes a nearly two-fold increase in the BFO–RGO electrode's specific capacitance.[117] Therefore, the use of a redox electrolyte may be promising to boost the electrochemical performance of SCs.

Conflicts of interest

There are no conflicts to declare.

Acknowledgements

This work was supported by the National Natural Science Foundation of China (No. 22072015).

References

1 Z. Guo, S. Zhao, T. Li, D. Su, S. Guo and G. Wang, *Adv. Energy Mater.*, 2020, **10**, 1903591.
2 L. Zu, W. Zhang, L. Qu, L. Liu, W. Li, A. Yu and D. Zhao, *Adv. Energy Mater.*, 2020, **10**, 2002152.
3 Y. Huang, M. Zhu, Y. Huang, Z. Pei, H. Li, Z. Wang, Q. Xue and C. Zhi, *Adv. Mater.*, 2016, **28**, 8344–8364.
4 J. Liang, B. Tian, S. Li, C. Jiang and W. Wu, *Adv. Energy Mater.*, 2020, **10**, 2000022.
5 J. Libich, J. Máca, J. Vondrák, O. Čech and M. Sedlaříková, *J. Energy Storage*, 2018, **17**, 224–227.
6 J. W. Long, D. Bélanger, T. Brousse, W. Sugimoto, M. B. Sassin and O. Crosnier, *MRS Bull.*, 2011, **36**, 513–522.
7 J. Liang, H. Zhao, L. Yue, G. Fan, T. Li, S. Lu, G. Chen, S. Gao, A. M. Asiri and X. Sun, *J. Mater. Chem. A*, 2020, **8**, 16747–16789.
8 J. Yan, S. Li, B. Lan, Y. Wu and P. S. Lee, *Adv. Funct. Mater.*, 2020, **30**, 1902564.
9 X. Lu, C. Wang, F. Favier and N. Pinna, *Adv. Energy Mater.*, 2017, **7**, 1601301.
10 Z. Zhai, W. Yan, L. Dong, J. Wang, C. Chen, J. Lian, X. Wang, D. Xia and J. Zhang, *Nano Energy*, 2020, **78**, 105193.
11 Y. Wang, L. Zhang, H. Hou, W. Xu, G. Duan, S. He, K. Liu and S. Jiang, *J. Mater. Sci.*, 2021, **56**, 173–200.
12 Y. Zhang, H. Feng, X. Wu, L. Wang, A. Zhang, T. Xia, H. Dong, X. Li and L. Zhang, *Int. J. Hydrogen Energy*, 2009, **34**, 4889.
13 D. Qu, *J. Power Sources*, 2002, **109**, 403.
14 R. S. Kate, S. A. Khalate and R. J. Deokate, *J. Alloys Compd.*, 2018, **734**, 89–111.
15 Y. Liu, Z. Wang, Y. Zhong, X. Xu, J.-P. M. Veder, M. R. Rowles, M. Saunders, R. Ran and Z. Shao, *Chem. Eng. J.*, 2020, **390**, 124645.
16 N. Choudhary, C. Li, J. Moore, N. Nagaiah, L. Zhai, Y. Jung and J. Thomas, *Adv. Mater.*, 2017, **29**, 1605336.
17 G. Wang, L. Zhang and J. Zhang, *Chem. Soc. Rev.*, 2012, **41**, 797–828.
18 Y. Zhai, Y. Dou, D. Zhao, P. F. Fulvio, R. T. Mayes and S. Dai, *Adv. Mater.*, 2011, **23**, 4828–4850.
19 H. Lv, Q. Pan, Y. Song, X.-X. Liu and T. Liu, *Nano-Micro Lett.*, 2020, **12**, 118.
20 M. Yu, Y. Lu, H. Zheng and X. Lu, *Chem. – Eur. J.*, 2018, **24**, 3639–3649.
21 Y. Shao, M. F. El-Kady, J. Sun, Y. Li, Q. Zhang, M. Zhu, H. Wang, B. Dunn and R. B. Kaner, *Chem. Rev.*, 2018, **118**, 9233–9280.
22 X. Lu, M. Yu, T. Zhai, G. Wang, S. Xie, T. Liu, C. Liang, Y. Tong and Y. Li, *Nano Lett.*, 2013, **13**, 2628–2633.
23 N. Choudhary, C. Li, J. Moore, N. Nagaiah, L. Zhai, Y. Jung and J. Thomas, *Adv. Mater.*, 2017, **29**, 1605336.
24 V. Augustyn, P. Simon and B. Dunn, *Energy Environ. Sci.*, 2014, **7**, 1597–1614.
25 W. Zhao, M. Jiang, W. Wang, S. Liu, W. Huang and Q. Zhao, *Adv. Funct. Mater.*, 2020, 2009136.
26 Z.-H. Huang, Y. Song, D.-Y. Feng, Z. Sun, X. Sun and X.-X. Liu, *ACS Nano*, 2018, **12**, 3557–3567.
27 G. Meng, Q. Yang, X. Wu, P. Wan, Y. Li, X. Lei, X. Sun and J. Liu, *Nano Energy*, 2016, **30**, 831–839.
28 V. D. Nithya and N. Sabari Arul, *J. Mater. Chem. A*, 2016, **4**, 10767–10778.
29 P. Tan, M. Liu, Z. Shao and M. Ni, *Adv. Energy Mater.*, 2017, **7**, 1602674.
30 X. Xu, W. Wang, W. Zhou and Z. Shao, *Small Methods*, 2018, **2**, 1800071.
31 J. T. Mefford, W. G. Hardin, S. Dai, K. P. Johnston and K. J. Stevenson, *Nat. Mater.*, 2014, **13**, 726–732.
32 Y. Liu, S. P. Jiang and Z. Shao, *Mater. Today Adv.*, 2020, **7**, 100072.
33 C. Chen, Y. Mei, Y. Huang and X. Hu, *Mater. Res. Bull.*, 2017, **96**, 365–371.
34 K. Brezesinski, J. Wang, J. Haetge, C. Reitz, S. O. Steinmueller, S. H. Tolbert, B. M. Smarsly, B. Dunn and T. Brezesinski, *J. Am. Chem. Soc.*, 2010, **132**, 6982–6990.
35 B. Mendoza-Sánchez and P. S. Grant, *Electrochim. Acta*, 2013, **98**, 294–302.
36 W. J. Yin, B. Weng, J. Ge, Q. Sun, Z. Li and Y. Yan, *Energy Environ. Sci.*, 2019, **12**, 442–462.
37 A. Kumar, A. Kumar and V. Krishnan, *ACS Catal.*, 2020, **10**, 10253–10315.

38 Q. Ji, L. Bi, J. Zhang, H. Cao and X. S. Zhao, *Energy Environ. Sci.*, 2020, **13**, 1408–1428.
39 J. Hwang, R. R. Rao, L. Giordano, Y. Katayama, Y. Yu and Y. Shao-Horn, *Science*, 2017, **358**, 751–756.
40 J. P. Attfield, P. Lightfoot and R. E. Morris, *Dalton Trans.*, 2015, **44**, 10541–10542.
41 V. M. Goldschmidt, *Naturwissenschaften*, 1926, **14**, 477–485.
42 R. Shannon, *Acta Crystallogr., Sect. A: Cryst. Phys., Diffr., Theor. Gen. Crystallogr.*, 1976, **32**, 751–767.
43 M. A. Peña and J. L. G. Fierro, *Chem. Rev.*, 2001, **101**, 1981–2018.
44 T. Jia, Z. Zeng, X. Zhang, P. Ohodnicki, B. Chorpening, G. Hackett, J. Lekse and Y. Duan, *Phys. Chem. Chem. Phys.*, 2019, **21**, 20454–20462.
45 M. Saiful Islam, *J. Mater. Chem.*, 2000, **10**, 1027–1038.
46 X. Huang, G. Zhao, G. Wang and J. T. S. Irvine, *Chem. Sci.*, 2018, **9**, 3623–3637.
47 S. Yoo, A. Jun, Y. W. Ju, D. Odkhuu, J. Hyodo, H. Y. Jeong, N. Park, J. Shin, T. Ishihara and G. Kim, *Angew. Chem., Int. Ed.*, 2014, **53**, 13064–13067.
48 D. Chen, C. Chen, Z. M. Baiyee, Z. Shao and F. Ciucci, *Chem. Rev.*, 2015, **115**, 9869–9921.
49 G. Gou, N. Charles, J. Shi and J. M. Rondinelli, *Inorg. Chem.*, 2017, **56**, 11854–11861.
50 R. Ceravola, J. Oró Solé, A. P. Black, C. Ritter, I. Puente Orench, I. Mata, E. Molins, C. Frontera and A. Fuertes, *Dalton Trans.*, 2017, **46**, 5128–5132.
51 A. A. Emery and C. Wolverton, *Sci. Data*, 2017, **4**, 170153.
52 G. Jácome-Acatitla, M. Álvarez-Lemus, R. López-González, C. García-Mendoza, A. Sánchez-López and D. Hernández-Acosta, *J. Photochem. Photobiol., A*, 2020, **390**, 112330.
53 J. Suntivich, H. A. Gasteiger, N. Yabuuchi, H. Nakanishi, J. B. Goodenough and Y. Shao Horn, *Nat. Chem.*, 2011, **3**, 546–550.
54 M. Retuerto, A. G. Pereira, F. J. Pérez-Alonso, M. A. Peña, J. L. G. Fierro, J. A. Alonso, M. T. Fernández-Díaz, L. Pascual and S. Rojas, *Appl. Catal., B*, 2017, **203**, 363–371.
55 Z. Du, P. Yang, L. Wang, Y. Lu, J. B. Goodenough, J. Zhang and D. Zhang, *J. Power Sources*, 2014, **265**, 91–96.
56 T. Shao, H. You, Z. Zhai, T. Liu, M. Li and L. Zhang, *Mater. Lett.*, 2017, **201**, 122–124.
57 Z. Li, W. Zhang, H. Wang and B. Yang, *Electrochim. Acta*, 2017, **258**, 561–570.
58 K. H. Ho and J. Wang, *J. Am. Ceram. Soc.*, 2017, **100**, 4629–4637.
59 T. Shao, H. You, Z. Zhai, T. Liu, M. Li and L. Zhang, *Mater. Lett.*, 2017, **201**, 122–124.
60 C. Sun, R. Hui and J. Roller, *J. Solid State Electrochem.*, 2010, **14**, 1125–1144.
61 Y. Zhang, J. Ding, W. Xu, M. Wang, R. Shao, Y. Sun and B. Lin, *Chem. Eng. J.*, 2020, **386**, 124030.
62 M. P. Harikrishnan and A. C. Bose, *AIP Conf. Proc.*, 2019, **2082**, 060001.
63 S. Hussain, M. S. Javed, N. Ullah, A. Shaheen, N. Aslam, I. Ashraf, Y. Abbas, M. Wang, G. Liu and G. Qiao, *Ceram. Int.*, 2019, **45**, 15164–15170.
64 N. K. Patel, R. G. Utter, D. Das and M. Pecht, *J. Power Sources*, 2019, **438**, 227040.
65 P. M. Wilde, T. J. Guther, R. Oesten and J. Garche, *J. Electroanal. Chem.*, 1999, **461**, 154–160.
66 M. Wohlfahrt-Mehrens, J. Schenk, P. M. Wilde, E. Abdelmula, P. Axmann and J. Garche, *J. Power Sources*, 2002, **105**, 182–188.
67 F. Xiao, X. Zhang, F. Hu and J. Zhang, *Mater. Chem. Phys.*, 2005, **94**, 221–225.
68 G. George, S. L. Jackson, C. Q. Luo, D. Fang, D. Luo, D. Hu, J. Wen and Z. Luo, *Ceram. Int.*, 2018, **44**, 21982–21992.
69 R. B. Rakhi, W. Chen, D. Cha and H. N. Alshareef, *Mater. Renewable Sustainable Energy*, 2013, **2**, 17.
70 A. K. Tomar, G. Singh and R. K. Sharma, *J. Power Sources*, 2019, **426**, 223–232.
71 Y. Zhu, X. Ji, Z. Wu, W. Song, H. Hou, Z. Wu, X. He, Q. Chen and C. E. Banks, *J. Power Sources*, 2014, **267**, 888–900.
72 Q. Wang, Z. Li, M. A. Bañares, L. T. Weng, Q. Gu, J. Price, W. Han and K. L. Yeung, *Small*, 2019, **15**, 1903525.
73 J. Chen, Z. He, G. Li, T. An, H. Shi and Y. Li, *Appl. Catal., B*, 2017, **209**, 146–154.
74 Q. Hu, B. Yue, F. Yang, H. Shao, J. Wang, L. Ji, Y. Jia, Y. Wang and J. Liu, *ChemistrySelect*, 2019, **4**, 11903–11912.
75 Q. Hu, B. Yue, H. Shao, F. Yang, J. Wang, Y. Wang and J. Liu, *J. Mater. Sci.*, 2020, **55**, 8421–8434.
76 Q. Pan, C. Yang, Q. Jia, W. Qi, H. Wei, M. Wang, S. Yang and B. Cao, *Chem. Eng. J.*, 2020, **397**, 125524.
77 S. Yin, Y. Wu, J. Chen, Z. Chen, H. Hou, Q. Liu, Y. Wang and W. Zhang, *Funct. Mater. Lett.*, 2018, **11**, 1850013.
78 C. D. Lokhande, T. P. Gujar, V. R. Shinde, R. S. Mane and S.-H. Han, *Electrochem. Commun.*, 2007, **9**, 1805–1809.
79 H.-Y. Kim, J. Shin, I.-C. Jang and Y.-W. Ju, *Energies*, 2020, **13**, 36.
80 N. Kitchamsetti, Y. R. Ma, P. M. Shirage and R. S. Devan, *J. Alloys Compd.*, 2020, **833**, 155134.
81 N. Kitchamsetti, R. J. Choudhary, D. M. Phase and R. S. Devan, *RSC Adv.*, 2020, **10**, 23446–23456.
82 M. A. Peña and J. L. G. Fierro, *Chem. Rev.*, 2001, **101**, 1981–2018.
83 B. C. Tofield and W. R. Scott, *J. Solid State Chem.*, 1974, **10**, 183–194.
84 T. Arakawa, N. Ohara and J. Shiokawa, *J. Mater. Sci.*, 1986, **21**, 1824–1827.
85 H. Wang, C. Tablet, A. Feldhoff and J. Caro, *Adv. Mater.*, 2005, **17**, 1785–1788.
86 Y. Teraoka, M. Yoshimatsu, N. Yamazoe and T. Seiyama, *Chem. Lett.*, 1984, 893–896.
87 J. Mizusaki, S. Yamauchi, K. Fueki and A. Ishikawa, *Solid State Ionics*, 1984, **12**, 119–124.
88 A. J. Hauser, R. E. Williams, R. A. Ricciardo, A. Genc, M. Dixit, J. M. Lucy, P. M. Woodward, H. L. Fraser and F. Yang, *Phys. Rev. B: Condens. Matter Mater. Phys.*, 2011, **83**, 014407.
89 W. Che, M. Wei, Z. Sang, Y. Ou, Y. Liu and J. Liu, *J. Alloys Compd.*, 2018, **731**, 381–388.
90 Y. Cao, B. Lin, Y. Sun, H. Yang and X. Zhang, *J. Alloys Compd.*, 2015, **638**, 204–213.
91 Z. A. Elsiddig, H. Xu, D. Wang, W. Zhang, X. Guo, Y. Zhang, Z. Sun and J. Chen, *Electrochim. Acta*, 2017, **253**, 422–429.
92 J. T. Mefford, X. Rong, A. M. Abakumov, W. G. Hardin, S. Dai, A. M. Kolpak, K. P. Johnston and K. J. Stevenson, *Nat. Commun.*, 2016, **7**, 11053.
93 H. Mo, H. Nan, X. Lang, S. Liu, L. Qiao, X. Hu and H. Tian, *Ceram. Int.*, 2018, **44**, 9733–9741.
94 X. W. Wang, Q. Q. Zhu, X. E. Wang, H. C. Zhang, J. J. Zhang and L. F. Wang, *J. Alloys Compd.*, 2016, **675**, 195–200.
95 X. Lang, H. Mo, X. Hu and H. Tian, *Dalton Trans.*, 2017, **46**, 13720–13730.
96 C. T. Alexander, J. T. Mefford, J. Saunders, R. P. Forslund, K. P. Johnston and K. J. Stevenson, *ACS Appl. Mater. Interfaces*, 2019, **11**, 5084–5094.
97 P. P. Ma, Q. L. Lu, N. Lei, Y. K. Liu, B. Yu, J. M. Dai, S. H. Li and G. H. Jiang, *Electrochim. Acta*, 2020, **332**, 135489.
98 A. Aguadero, D. Pérez-Coll, J. A. Alonso, S. J. Skinner and J. Kilner, *Chem. Mater.*, 2012, **24**, 2655–2663.
99 M. A. Salguero Salas, J. M. De Paoli, O. E. Linarez Pérez, N. Bajales and V. C. Fuertes, *Microporous Mesoporous Mater.*, 2020, **293**, 109797.
100 A. K. Tomar, G. Singh and R. K. Sharma, *ChemSusChem*, 2018, **11**, 4123–4130.
101 L. Zhu, Y. Liu, C. Su, W. Zhou, M. Liu and Z. Shao, *Angew. Chem., Int. Ed.*, 2016, **55**, 9576–9579.
102 Y. Yan, T. Wang, X. Li, H. Pang and H. Xue, *Inorg. Chem. Front.*, 2017, **4**, 33–51.
103 H. Xia, C. Hong, X. Shi, B. Li, G. Yuan, Q. Yao and J. Xie, *J. Mater. Chem. A*, 2015, **3**, 1216–1221.
104 X. Lang, X. Sun, Z. Liu, H. Nan, C. Li, X. Hu and H. Tian, *Mater. Lett.*, 2019, **243**, 34–37.
105 P. Liu, J. Liu, S. Cheng, W. Cai, F. Yu, Y. Zhang, P. Wu and M. Liu, *Chem. Eng. J.*, 2017, **328**, 1–10.
106 Y. Cao, B. Lin, Y. Sun, H. Yang and X. Zhang, *Electrochim. Acta*, 2015, **178**, 398–406.
107 Z. S. Wu, W. Ren, D. W. Wang, F. Li, B. Liu and H. M. Cheng, *ACS Nano*, 2010, **4**, 5835–5842.
108 H. Jiang, Y. Dai, Y. Hu, W. Chen and C. Li, *ACS Sustainable Chem. Eng.*, 2014, **2**, 70–74.
109 J. Lv, Y. Zhang, Z. Lv, X. Huang, Z. Wang, X. Zhu and B. Wei, *Electrochim. Acta*, 2016, **222**, 1585–1591.
110 K. Chen and D. Xue, *J. Colloid Interface Sci.*, 2015, **446**, 77–83.
111 N. Maheswari and G. Muralidharan, *Dalton Trans.*, 2016, **45**, 14352–14362.

112 S. Nagamuthu, S. Vijayakumar and K. S. Ryu, *Mater. Chem. Phys.*, 2017, **199**, 543–551.
113 X. Lang, H. Zhang, X. Xue, C. Li, X. Sun, Z. Liu, H. Nan, X. Hu and H. Tian, *J. Power Sources*, 2018, **402**, 213–220.
114 M. D. Stoller, S. Park, Y. Zhu, J. An and R. S. Ruoff, *Nano Lett.*, 2008, **8**, 3498–3502.
115 Y. Sun, Q. Wu and G. Shi, *Energy Environ. Sci.*, 2011, **4**, 1113–1132.
116 J. Hu, L. Wang, L. Shi and H. Huang, *J. Power Sources*, 2014, **269**, 144–151.
117 D. Moitra, C. Anand, B. K. Ghosh, M. Chandel and N. N. Ghosh, *ACS Appl. Energy Mater.*, 2018, **1**, 464–474.
118 A. Galal, H. K. Hassan, T. Jacob and N. F. Atta, *Electrochim. Acta*, 2018, **260**, 738–747.
119 H. Pan, C. K. Poh, Y. P. Feng and J. Lin, *Chem. Mater.*, 2007, **19**, 6120–6125.
120 D. Hulicova, M. Kodama and H. Hatori, *Chem. Mater.*, 2006, **18**, 2318–2326.
121 A. Rezanezhad, E. Rezaie, L. S. Ghadimi, A. Hajalilou, E. Abouzari-Lotf and N. Arsalani, *Electrochim. Acta*, 2020, **335**, 135699.
122 Z. A. Elsiddig, D. Wang, H. Xu, W. Zhang, T. Zhang, P. Zhang, W. Tian, Z. Sun and J. Chen, *J. Alloys Compd.*, 2018, **740**, 148–155.
123 P. M. Shafi, V. Ganesh and A. C. Bose, *ACS Appl. Energy Mater.*, 2018, **1**, 2802–2812.
124 S. Choi, S. Yoo, J. Kim, S. Park, A. Jun, S. Sengodan, J. Kim, J. Shin, H. Y. Jeong, Y. Choi, G. Kim and M. Liu, *Sci. Rep.*, 2013, **3**, 2426.
125 A. Chroneos, B. Yildiz, A. Tarancón, D. Parfitt and J. A. Kilner, *Energy Environ. Sci.*, 2011, **4**, 2774–2789.
126 B. P. Uberuaga and G. Pilania, *Chem. Mater.*, 2015, **27**, 5020–5026.
127 E. G. Steward and H. P. Rooksby, *Acta Crystallogr.*, 1951, **4**, 503–507.
128 J. Singh, A. Kumar and U. K. Goutam, *Appl. Phys. A: Mater. Sci. Process.*, 2020, **126**, 11.
129 J. Singh, U. K. Goutam and A. Kumar, *Solid State Sci.*, 2019, **95**, 105927.
130 A. Kumar, A. Kumar and A. Kumar, *Solid State Sci.*, 2020, **105**, 106252.
131 Z. Meng, J. Xu, P. Yu, X. Hu, Y. Wu, Q. Zhang, Y. Li, L. Qiao, Y. Zeng and H. Tian, *Chem. Eng. J.*, 2020, **400**, 15966.
132 M. Alam, K. Karmakar, M. Pal and K. Mandal, *RSC Adv.*, 2016, **6**, 114722–114726.
133 Y. Liu, Z. Wang, J. P. M. Veder, Z. Xu, Y. Zhong, W. Zhou, M. O. Tade, S. Wang and Z. Shao, *Adv. Energy Mater.*, 2018, **8**, 1702604.
134 A. A. Taskin, A. N. Lavrov and Y. Ando, *Appl. Phys. Lett.*, 2005, **86**, 091910.
135 C. Bernuy-Lopez, K. Høydalsvik, M. A. Einarsrud and T. Grande, *Materials*, 2016, **9**, 154.
136 Z. Wang, Y. Liu, Y. Chen, L. Yang, Y. Wang and M. Wei, *J. Alloys Compd.*, 2019, **810**, 151830.
137 Z. Xu, Y. Liu, W. Zhou, M. O. Tade and Z. Shao, *ACS Appl. Mater. Interfaces*, 2018, **10**, 9415–9423.
138 A. K. Tomar, A. Joshi, S. Atri, G. Singh and R. K. Sharma, *ACS Appl. Mater. Interfaces*, 2020, **12**, 15128–15137.
139 P. L. Wise, I. M. Reaney, W. E. Lee, T. J. Price, D. M. Iddles and D. S. Cannell, *J. Eur. Ceram. Soc.*, 2001, **21**, 2629–2632.
140 P. L. Wise, I. M. Reaney, W. E. Lee, T. J. Price, D. M. Iddles and D. S. Cannell, *J. Eur. Ceram. Soc.*, 2001, **21**, 1723–1726.
141 Z. Sang, W. Che, S. Yang and Y. Liu, *Mater. Lett.*, 2018, **217**, 23–26.
142 M. Wei, W. Che, H. Li, Z. Wang, F. Yan, Y. Liu and J. Liu, *Appl. Surf. Sci.*, 2019, **484**, 551–559.
143 H.-s. Nan, X.-y. Hu and H.-w. Tian, *Mater. Sci. Semicond. Process.*, 2019, **94**, 35–50.
144 C. A. Hancock, J. M. Porras-Vazquez, P. J. Keenan and P. R. Slater, *Dalton Trans.*, 2015, **44**, 10559–10569.
145 J. F. Shin, A. Orera, D. C. Apperley and P. R. Slater, *J. Mater. Chem.*, 2011, **21**, 874–879.
146 J. Ran, T. Wang, J. Zhang, Y. Liu, C. Xu, S. Xi and D. Gao, *Chem. Mater.*, 2020, **32**, 3439–3446.
147 X. Xu, Y. Pan, Y. Zhong, R. Ran and Z. Shao, *Mater. Horiz.*, 2020, **7**, 2519–2565.
148 L. Zhu, R. Ran, M. Tadé, W. Wang and Z. Shao, *Asia-Pac. J. Chem. Eng.*, 2016, **11**, 338–369.